THE JOURNAL OF PHYSICAL CHEMISTRY C

C: Plasmonics; Optical, Magnetic, and Hybrid Materials

Hot Carrier Generation in Two-Dimensional Silver Nanoparticle Array at Different Excitation Wavelengths Under On-Resonant Condition

Yuki Takeuchi, Antoine Violas, Tetsuya Fujita, Yasuaki Kumamoto, Mircea Modreanu, Takuo Tanaka, Katsumasa Fujita, and Nobuyuki Takeyasu

J. Phys. Chem. C, **Just Accepted Manuscript** • DOI: 10.1021/acs.jpcc.0c04034 • Publication Date (Web): 30 May 2020

Hot carrier generation in two-dimensional silver nanoparticle array at different excitation wavelengths under on-resonant condition

Yuki Takeuchi,[†] Antoine Violas,[†,‡] Tetsuya Fujita,[†] Yasuaki Kumamoto,[§,⊥] Mircea Modreanu,[∥] Takuo Tanaka,[#,▽,¶] Katsumasa Fujita[§] and Nobuyuki Takeyasu[†,*]

[†] Graduate School of Natural Science and Technology, Okayama University, 3-1-1, Tsushima-naka, Kita-ku, Okayama 700-8530 Japan

[‡] Sorbonne Université - UPMC, Univ. Paris 06, UFR 925, Paris, France

[§] Department of Applied Physics, Faculty of Engineering, Osaka University, 2-1, Yamadaoka, Suita, Osaka 565-0871, Japan

[⊥] Department of Pathology and Cell Regulation, Graduate School of Medical Sciences, Kyoto Prefectural University of Medicine, 465 Kajiicho, Kawaramachi-Hirokoji, Kamigyo-ku, Kyoto, Kyoto 602-8566, Japan.

[∥] Tyndall National Institute, University College Cork, Lee Maltings, Dyke Parade, Cork, T12 R5CP, Ireland.

[#] Metamaterials Laboratory, RIKEN Cluster for Pioneering Research, 2-1, Hirosawa, Wako, Saitama 351-0198, Japan

[▽] Innovative Photon Manipulation Research Team, RIKEN Center for Advanced Photonics, 2-1, Hirosawa, Wako, Saitama 351-0198, Japan

[¶] Institute of Post-LED Photonics, Tokushima university, 2-1, Minamijosanjima, Tokushima 770-8506, Japan

* Corresponding author: takeyasu@okayama-u.ac.jp, +81-(0)86-251-7845

ABSTRACT

We evaluated the hot carrier generation in two-dimensional (2D) silver nanoparticle arrays under light illumination at different wavelengths, 458, 532, 671 and 785 nm. The 2D silver nanoparticle arrays were tailored to match the plasmon resonance to each excitation wavelength in order to fulfil the on-resonant condition. We selected *para*-aminothiophenol (*p*-ATP) as a probe molecule, which is chemically transformed into 4,4'-dimercaptoazobenzene (DMAB) upon light illumination. The reaction is driven by hot carriers emitted from plasmonic surface. For evaluation of hot carrier-generation, we monitored chemical transformation from *p*-ATP into DMAB with surface-enhanced Raman scattering (SERS). The normalized Raman intensity of DMAB was plotted against the total exposure, where the peak intensity increased as the total exposure increased due to the increase of the number of DMAB molecules. The saturation of the peak growth was observed, representing the chemical transformation was completed, at different exposures for each wavelength. The total exposure required for completing the chemical transformation was smaller at 458 nm by at least ~10^5 times than that at 785 nm although the difference of the photon energy was only 1.7 times. The growth of the Raman peak was related to the laser intensity as well, where the higher laser intensity showed more rapid growth. These results indicated that more hot carriers with the sufficient energy for the chemical transformation were generated at the shorter excitation wavelength as well as at the higher laser intensity.

KEY WORDS

hot carriers, plasmon-mediated chemical reaction, excitation wavelength dependence, SERS, on-resonant condition, silver nanoparticle array

MAIN TEXT

1. Introduction

Light is confined at the metallic nanostructures through the coupling to collective oscillations of the free-electrons as surface plasmon polaritons (SPPs).[1] The nano-confinement of light enabled unprecedented applications, such as surface-/tip-enhanced Raman scattering (SERS/TERS).[2-8] It has been also widely recognized that hot carriers, which are energetic electrons and holes, are generated in the metallic nanostructures under light illumination.[9] The generated hot electrons can be monitored as photocurrent, which is observed when the incident photon energy exceeds the barrier energy of the semiconductor/insulator, with the metallic nanostructures.[10,11] For practical applications of hot carriers, it is important to understand the density and energetic profiles of the hot carriers in metals, which have been numerically studied.[12-15] It has been reported that the energy distribution and scattering process of the hot carriers generated by SPPs in noble metals is different between below and above the interband transition threshold, where intraband excitation results in the longer lifetime of hot carriers compared to interband excitation.[12,13] Decay of the hot electrons was experimentally studied, where the electron-phonon coupling time was measured for gold nanoparticles by transient absorption spectroscopy.[16] Clear difference was observed in the relaxation of hot carriers in gold nanoparticles between the intraband and the interband excitations although no wavelength dependence was observed in each excitation.

Hot electrons are also able to induce chemical reactions, such as oxidation, dissociation of hydrogen and so on, at the surface of the metallic nanostructures.[17-20] Christopher *et al*. have reported catalytic oxidation such as epoxidation of ethylene on silver nanocubes, where the normalized photocatalytic rate depends on plasmon intensity although the excitation wavelength dependence of the reaction rate was not clearly observed.[17] Many attempts have been made to understand the plasmon-mediated chemical reaction with SERS enabling the monitoring of the chemical transformation of molecular structure when the molecules are bound to the surface. *para*-Aminothiophenol (*p*-ATP) has been especially studied, which is chemically transformed into 4,4'-dimercaptoazobenzene (DMAB) during SERS measurement.[21-32] The reaction may depend on the resonant condition. For example, Wang *et al*. have investigated plasmon driven surface catalysis reaction of *p*-ATP to DMAB in Au/Ag nanoparticle-film gaps.[26] The SERS measurements were performed by excitation wavelength of 532 nm and 633 nm. Their results imply more confined energy at the gaps drives the reaction more efficiently due to the plasmon resonance. The tendency appeared in both cases of 532 nm and 633 nm although wavelength dependence was not clearly explained using substrates with same

material and resonant condition. Huang *et al*. have reported wavelength-dependent SERS study on Au film/PATP/Au NP junctions with same incident laser intensity.[27] It was found that the yield of DMAB is consistent with the order of electric field enhancement at the junction. On the other hand, it has been reported that the reaction seems to be influenced also by photon energy. Kang *et al.* reported that the 532 nm excitation laser shortened time of the reaction from *p*-ATP to DMAB compared to the 633 nm excitation, where the SERS measurements were performed on the hierarchical Ag microspheres.[30] Dong *et al.* have reported wavelength-dependent catalytic reaction on Au, Ag and Cu films.[31] Ye *et al.* have also investigated the excitation wavelength dependence on gold nanorings with the plasmon resonance at 800 nm.[32] From those reports, the reaction rate tends to slow down as the excitation wavelength increases, in other words, these results indicate higher energy photons may drive the plasmon-mediated photocatalysis more efficiently, despite the wavelength dependence has not yet been quantified. So, in this article, we systematically evaluated the dependence of the hot carrier generation on the excitation wavelength at silver nano-surface by monitoring the chemical transformation of *p*-ATP with SERS. The carrier dynamics is different between the interband and intraband excitations, and is influenced also by other factors.[13,14] The excitation lasers were 458, 532, 671 and 785 nm, which were below the interband transition threshold for silver.[12,13] 2D silver nanoparticle (AgNP) arrays were tailored to the individual excitation wavelengths, which was "on-resonant" condition, enabling more quantitative discussion about the generated hot electrons at the different excitation wavelengths since it is known that hot carrier generation is maximized under resonance.[10]

2. Experimental section

2.1 Fabrication of 2D AgNP array

The 2D AgNP array was tailored to each excitation wavelength without changing the size of the AgNPs, as reported elsewhere.[33] Silver seed solution was prepared by mixing 37.5 mL of water, 0.85 mL of $AgNO_3$ aqueous solution (1.0 w/v%), 10.0 mL of trisodium citrate aqueous solution (1.0 w/v%) and 1.0 mL of $NaBH_4$ aqueous solution (0.1 w/v%), and the mixed solution was kept at 70ºC for an hour. The Ag seed solution (5.0 mL) was mixed with 37.5 mL of water and 1.0 mL of trisodium citrate aqueous solution (1.0 w/v%) and heated at the boiling point. Furthermore, 0.85 mL of $AgNO_3$ aqueous solution (1.0 w/v%) was added and heated for an hour. After heating, 1.0 mL of trisodium citrate aqueous solution (1.0 w/v%) and 0.85 mL of $AgNO_3$ aqueous solution (1.0 w/v%) were added and heated for an hour again, resulting 30-40 nm of AgNPs. The AgNP solution was mixed with oil-in-water emulsion prepared with water, *n*-hexane and decylamine.

Instead of decylamine, stearylamine was used for 2D AgNP arrays at 458 nm excitation. AgNP array was self-assembled at the interface between *n*-hexane and water, and it was transferred to the glass substrate.

2.2 SERS measurement

2.2.1 SERS sample preparation

p-ATP (97.0%, 1st grade) was purchased from Wako. *p*-ATP ethanol solution (1.0 mM) was prepared as a sample solution. The solution (0.02 mL) was dropped and dried on the 2D AgNP array, and then SERS measurement was performed on the AgNP array.

2.2.2 SERS measurements at different laser intensities

SERS spectra of *p*-ATP were measured at different four excitation lasers, 785 nm, 671 nm, 532 nm and 458 nm. For 785 nm and 532 nm excitations, the measurements were performed with a Raman microscope (NRS-5100, JASCO). The numerical aperture (NA) of the objective lens (20X) was 0.45. The SERS spectra were measured with the laser intensities estimated as 0.033, 0.33 and 3.3 kW/mm^2, respectively. The measuring time was 20 s. Similarly, the measurements for 532 nm excitation were performed at the laser intensities of 2.3, 23 and 2.3 × 10^2 W/mm^2 and the measuring time of 40 s. For 671 nm excitation, the measurements were performed with a Raman microscope (Raman-11, Nanophoton). The NA of the objective lens (20X) was 0.75. The excitation laser intensities were 0.012, 0.12 and 1.2 kW/mm^2 and the measurement time was 5 s. For 458 nm excitation, we used a home-built micro-Raman spectrometer. Briefly, the beam emitting from argon ion laser was expanded and collimated to fill the pupil of an objective lens (40X/NA0.6). The objective lens focused the beam on a sample located on an XY manual stage. Raman scattering from the sample was collected with the objective lens and was guided to a Czerny-Turner spectrometer (SP-2500, Acton), equipped with an entrance slit (50 μm in width), a blazed grating (600 lines/mm), and a cooled CCD camera (ProEM 16004, Princeton Instruments). Prior to entrance to the spectrometer, the beam was filtered with a longwave-pass edge filter. The spectrometer was calibrated by a halogen lamp and Raman scattering bands of ethanol in intensity and wavenumber axes, respectively. A mechanical shutter was located at the excitation path and was synchronized with the CCD camera so that the sample irradiation time and the signal accumulation time were fairly regulated. The excitation laser intensities were 4.4, 8.8, and 44 W/mm^2 and the total exposure time was 2 s.

2.2.3 Comparison of reaction rate among different excitation SERS measurements

To evaluate the reaction rates, the SERS measurements of *p*-ATP were iterated at an identical position in each measurement condition. Iterations were 30 for 785 nm excitation, 10 for 671 nm, 25 for 532 nm and 20 for 458 nm. To understand influence of photon density on the reaction rate, we varied laser intensity together with measurement time while keeping total exposure (i.e., product of laser intensity and measurement time) constant; for 785 nm the laser intensities were 3.30×10^2, 1.65×10^3 and 3.30×10^3 W/mm^2 and the measurement times were 100, 20 and 10 s; for 671 nm the laser intensities were 58.0, 1.16×10^2 and 1.16×10^3 W/mm^2 and the measurement times were 20, 10 and 1 s; for 532 nm the laser intensities were 2.6, 26 and 2.6×10^2 W/mm^2 and the measurement times 10, 1 and 0.1 s; for 458 nm the laser intensities were 4.4, 8.8 and 44 W/mm^2 and the measurement times were 2, 1 and 0.2 s.

2.3 DDA simulation

We used discrete dipole approximation (DDA, ver. 7.3.2) for the simulations of the extinction spectra and the electric field distribution on the two-dimensional silver nanoparticle (AgNP) array. AgNPs (D = 40 nm) were aligned hexagonally in plane (yz-plane) with the inter-particle gap, G (6, 4, 2 and 1 nm). The total number of AgNPs was fixed to be 30. The distance between each dipole consisting of the AgNP was 1 nm (See also SI, SFig. 1). The incident angle of the electromagnetic wave was normal to the AgNP array (along the x-axis), where the electric vector was oriented to y-axis. The ambient condition was supposed to be vacuum (the refractive index: n = 1). The dielectric function of silver was referred to Ref. 34.

3. Result & Discussion

3.1 SERS spectra of *p*-ATP at 785 nm, 671 nm, 532 nm and 458 nm

Figure 1 shows the extinction spectra of the 2D AgNP arrays on glass substrates used as SERS active substrates at 458, 532, 671 and 785 nm. For those substrates, the resonance peaks were tailored by controlling the inter-particle gaps although the size range of the AgNPs was constant (30-40 nm), e.g., the extinction peaks were red shifted approximately to 720 nm by shortening the inter-particle gap for the 671 and 785 nm excitations. The extinctions of four films are ~0.19, ~0.56, ~0.66 and ~0.76 at the resonant wavelengths of 530 nm, 570 nm, 740 nm and 740 nm, respectively.

The plasmon peak of each SERS substrate fairly matched with each excitation wavelength and this matching means that all measurements were performed under "on-resonant" conditions. The extinctions are ~0.15 (~70% in transmittance), ~0.54 (~29% in transmittance), ~0.62 (~24% in transmittance) and ~0.74 (~18% in transmittance) at the excitation wavelengths of 458 nm, 532 nm, 671 nm and 785 nm, respectively. The difference of the extinction was derived from multi-layered structures between 671 and 785 nm.

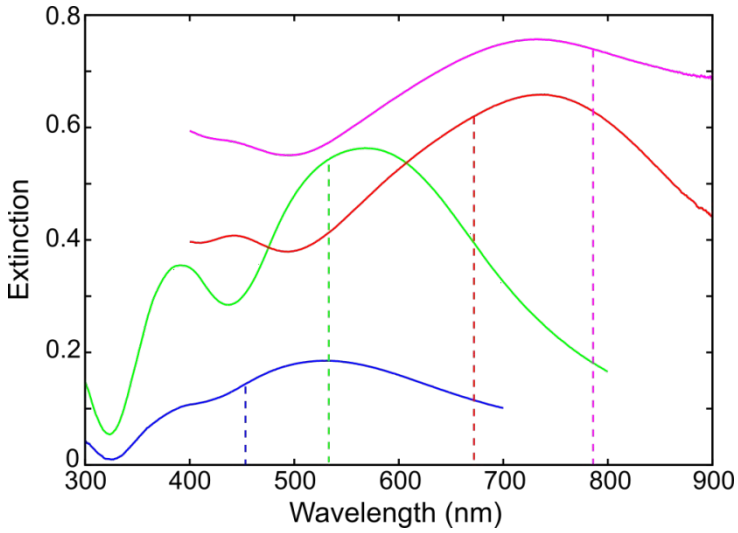

Figure 1. Extinction spectra of SERS active substrates fabricated for different excitation wavelengths, 458 (blue), 532 (green), 671 (red) and 785 (magenta) nm. Broken lines indicate the excitation wavelengths.

SERS spectra of *p*-ATP were measured at 458, 532, 671 and 785 nm on 2D AgNP array under on-resonant conditions. *p*-ATP is transparent at the excitation wavelengths (See also SI, SFig.2), and this fact indicates that surface-enhanced Raman scattering occurred at electronically non-resonant conditions for all the excitation wavelengths. A 785 nm excitation SERS spectrum of *p*-ATP measured at 0.033, 0.33 and 3.3 kW/mm^2 is shown in Fig. 2(a). S-C bond was clearly observed at 1080 cm^{-1} for all the intensities because of the electromagnetic enhancement. Beside this band characteristic for *p*-ATP, other Raman peaks appeared at 1140, 1390 and 1430 cm^{-1} at 0.33 and 3.3 kW/mm^2, reflecting the production of DMAB. Furthermore, peak shift was observed from 1590 cm^{-1} to 1575 cm^{-1} as the laser intensities increased, where those peaks at 1590 cm^{-1} and 1575 cm^{-1} are originated from *p*-ATP and DMAB, respectively.[21,35] The peak shift may reflect the change in the number of *p*-ATP. The peak at 1180 cm^{-1} can be assigned to combination of C-N stretching and C-H bending. This peak should be observed in both *p*-ATP and

DMAB.[35] Similar measurements were performed at 671 nm excitation, whose results are shown in Fig. 2(b). The Raman peaks assigned to DMAB were clearly observed only at 1.2 kW/mm^2.

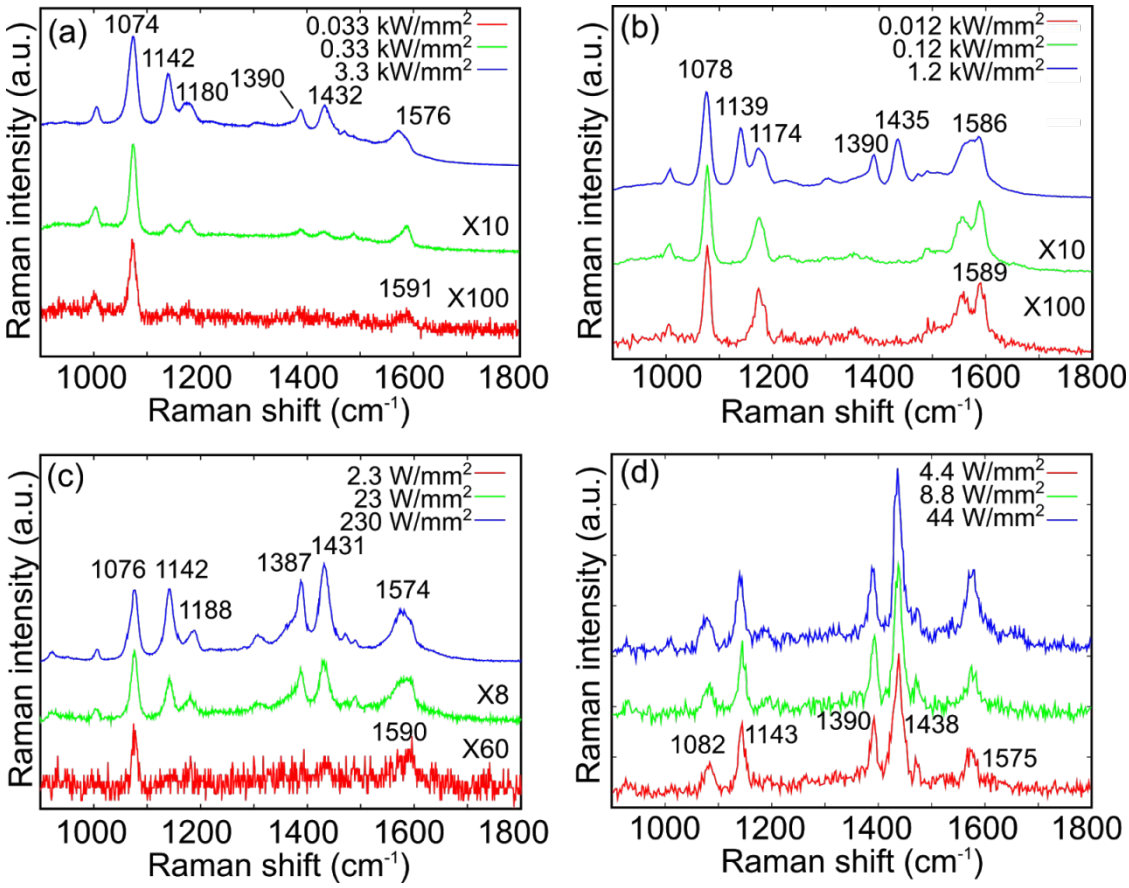

Figure 2. SERS spectra of *p*-ATP measured at (a) 785, (b) 671, (c) 532 and (d) 458 nm with different laser intensities under on-resonant conditions. The Raman peak observed at 1556 cm^{-1} was derived from atmospheric oxygen.

Figure 2(c) shows the SERS spectra measured at 532 nm excitation. The Raman peaks of DMAB were clearly observed even at the laser intensity of 23 W/mm^2. Figure 2(d) shows the SERS spectra measured at 458 nm excitation. It was confirmed that the peak of S-C bond has identical shape as well as other excitations, in spite of the peak appeared broad due to small S/N ratio (See also SI, SFig.3). Also, the relative of three peaks at 458 nm is considerably difference compared to other excitations since DMAB might absorb the light at the wavelength of 458 nm due to isomerization, where resonant Raman scattering was observed.[36] It was found that DMAB was similarly produced even at 4.4 W/mm^2. The reaction seems to be completed at the laser intensity because almost no

change was observed in the shape of the Raman spectra at 4.4, 8.8 and 44 W/mm^2. From these results, it was found that the chemical transformation from *p*-ATP to DMAB occurred for all excitation wavelengths, generating three Raman peaks at 1140, 1390 and 1430 cm^{-1}. However, the laser intensity more than 0.1 kW/mm^2 was required for observing the Raman signals with the measuring time of 20 s at 785 nm while several W/mm^2 was sufficient with the exposure time of 2 s at 458 nm, indicating the generation of the Raman peaks were affected by not only the laser intensity but also the excitation wavelength.

3.2 Quantitative analysis of SERS peak and hot carrier generation

In the previous section, we showed the chemical transformation from *p*-ATP to DMAB monitored with SERS. *p*-ATP is transformed into DMAB, and the number of DMAB molecules increases according to the exposure, leading to the growth of the Raman peaks of DMAB. We focused on the SERS peak of DMAB at 1140 cm^{-1}, and investigated the peak growth against the exposure. We iterated SERS measurements of *p*-ATP at the same position, laser intensity, and exposure time. The Raman intensity of DMAB at 1140 cm^{-1}, I_{1140}, increases because the number of DMAB molecules increases due to the chemical transformation as the total exposure increases. The peak intensity was normalized by the peak intensity at 1080 cm^{-1}, I_{1140}/I_{1080}, for compensation of the Raman cross-sections among the different excitation wavelengths. We chose I_{1080} as a standard for normalization because it is less affected by the chemical reaction since the S-C bond does not change before and after the chemical reaction. We expected that as the total exposure increases the chemical reaction progresses and consequently I_{1140}/I_{1080} increased even at the same intensity of the excitation laser.

Figure 3 shows the relationships between the total exposure and I_{1140}/I_{1080} for 785, 671, 532 and 458 nm excitations. Figure 3(a) shows the results for 785 nm excitation at 330, 1650 and 3300 W/mm^2. It was observed that I_{1140}/I_{1080} increased according to the total exposure, indicating the increase of the number of DMAB molecules through the chemical transformation. We changed the exposure time according to the laser intensity in order to keep the total exposure constant, as mentioned in the section of 2.2.3. The production of DMAB molecules should be same for the all laser intensities because the total exposures were constant. However, I_{1140}/I_{1080} was different at each laser intensity, indicating the number of the produced DMAB molecules was different. I_{1140}/I_{1080} was larger for the higher laser intensity. The fact is consistent with previous results.[25] Similar results were obtained also at 671 and 532 nm excitations, as shown in Fig. 3(b,c). From these results, the higher intensity is effective for inducing the chemical reaction. The

intensity dependence of the chemical reaction can be explained by competition of the hot carrier generation against the relaxation process.[9] For 458 nm, I_{1140}/I_{1080} were almost the same, ~2, regardless of laser intensity although the laser intensities were similar to the 532 nm measurements. The result implied that the chemical transformation seemed to be completed even at the first exposure of 4.4 W/mm^2.

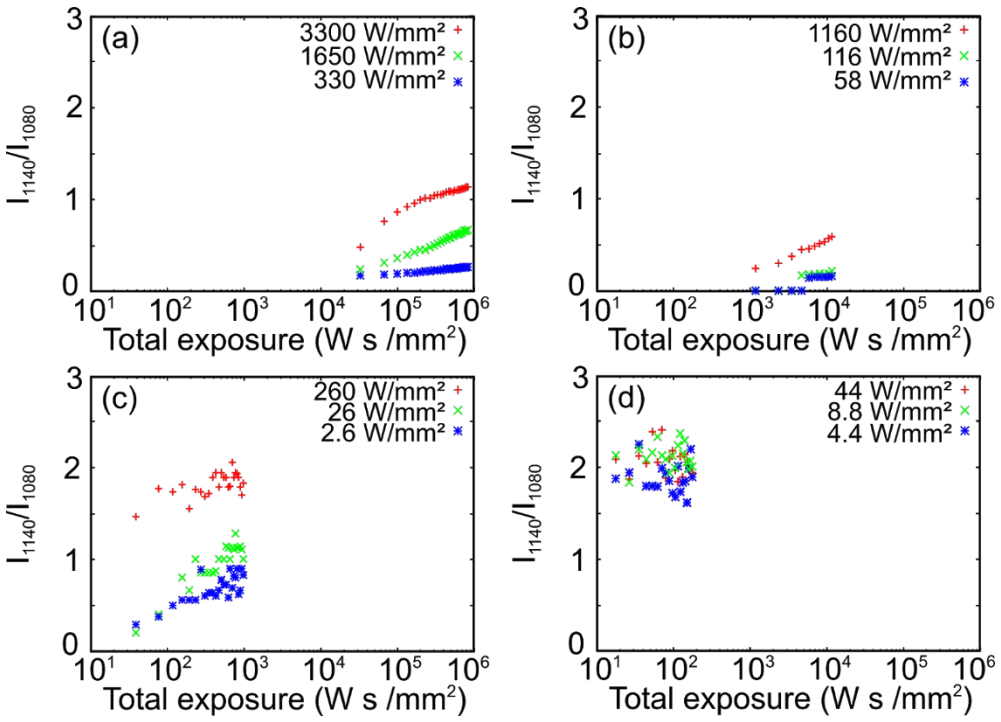

Figure 3. Relationship between total exposure and peak intensity at 1140 cm^{-1} at different laser intensities for (a) 785 nm, (b) 671 nm, (c) 532 nm and (d) 458 nm excitations, where I_{1140} is normalized by I_{1080}.

Saturation of I_{1140}/I_{1080} indicated completion of the chemical transformation. The chemical transformation seemed to be completed at the exposure of 10^6 Ws/mm^2 (3300 W/mm^2) for 785 nm. The laser intensity was reduced to < 260 W/mm^2 for 532 nm excitation, and the completion of the chemical transformation was observed at 1.0×10^3 Ws/mm^2. For 458 nm, I_{1140}/I_{1080} seemed to be saturated even at 1.0×10 Ws/mm^2 (4.4 W/mm^2). These results indicated that the total exposure required for completion of the chemical transformation was different at each excitation wavelength, where the required exposure was smaller for the shorter wavelength. The required exposure at 458 (2.71 eV) nm was smaller by at least ~10^5 times compared to 785 nm (1.58 eV). The tendency that shorter wavelength induces the reaction more efficiently is consistent with previous

results.[30-32] However, in our case, the wavelength dependence of the reaction was evaluated by same AgNPs under on-resonant conditions for all excitation wavelengths. It can be said that this is a new finding of wavelength dependence compared with the results reported so far.

3.3 Simulations for electric field enhancement for 458 nm and 532 nm

No wavelength dependence was reported in electron-phonon coupling in intraband excitation,[16] however, dependence of the reaction rate on the excitation wavelength was clearly observed in our experiment. The AgNP size was constant in the experiment, therefore, the inter-particle gap was changed for the tuning of the plasmon resonance. It is considered that the wider inter-particle gap may lead to deterioration of the hot carrier generation because light absorption should be proportional to the square of the electric field (E^2). Therefore, it may be significant to estimate the electric field at the interparticle gaps. Here, we calculated the extinction spectra of the AgNP (40 nm) arrays with different inter-particle gap (G= 6, 4, 2 and 1 nm). Furthermore, the field distributions were also calculated at each plasmon resonance.

The calculation model is shown in Fig. 4(a) (See also SI, SFig. 1 and SFig. 4). Figure 4(b) shows the calculated extinction spectra (See also SI, SFig. 4 for the absorption and scattering components). The calculated extinction spectra at different Gs have two peaks. These peaks reflect the plasmon modes hybridized from electric dipoles induced in each AgNPs.

The extinction peaks were found at 448, 472, 544 and 548 nm for G = 6, 4, 2 and 1 nm, respectively. The absorption peaks were slightly different from the extinction peaks, which were 448, 484, 532 and 576 nm, respectively. These slight differences derive from the difference in shape of scattering and absorption spectrum. From comparison with the experimental result of the extinction spectrum (Fig. 1), the inter-particle gap was estimated to be 2~4 nm for 458 nm excitation.

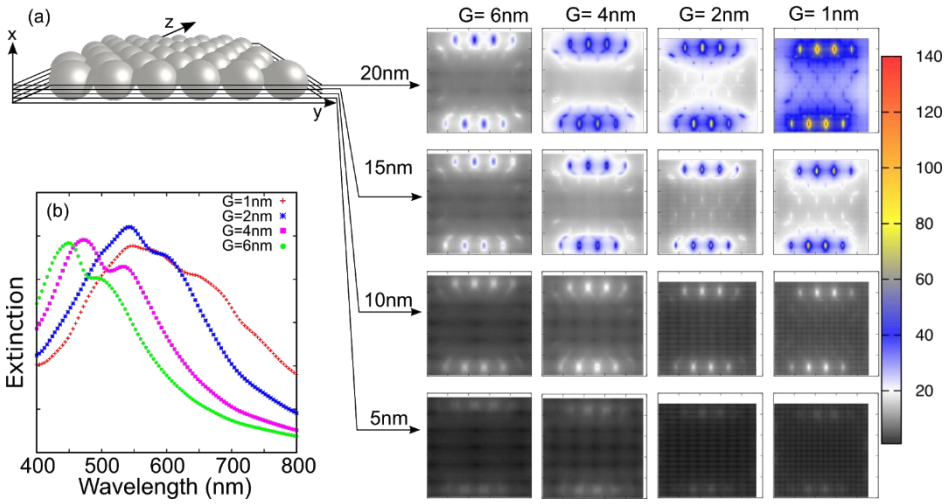

Figure 4. (a) Model for DDA simulation. AgNPs (D = 40 nm) are hexagonally aligned in yz-plane. The inter-particle gap (G) was changed at 6, 4, 2 and 1 nm. Electric field distributions ($|E/E_0|^2$) of AgNP array at x = 5, 10, 15 and 20 nm for each G when the array is illuminated by the excitation wavelength at the absorption maximum. The scale of each graph is 250 × 250 nm^2. (b) Calculated extinction spectra at different Gs (6, 4, 2 and 1 nm).

Furthermore, we calculated the field enhancement distribution ($|E/E_0|^2$) over the whole AgNP array structure at the absorption peaks for each G. Figure 4(a) also shows the field distributions in yz-planes at x = 5, 10, 15 and 20 nm, where the bottom and middle of the AgNP array are x= 0 and 20 nm, respectively. For G = 4 nm, ~70 fold enhancement was achieved at x = 20 nm. For G = 2 nm, the field enhancement increased up to ~100. From the calculation result, larger absorption is expected at 532 nm because the absorption should be proportional to the square of the electric field. However, the experimental results indicated that the hot carriers were generated more efficiently at 458 nm. The complex permittivity is -11+0.33i at 2.38 eV (521 nm), and -7+0.21i at 2.75 eV (450 nm).[37] Therefore, the shorter wavelength can penetrate more deeply into the metal. From the calculations, it was also found that the area of the higher electric field was larger at x = 15 and 10 nm for G = 4 nm compared to G = 2 nm, which may be the origin for generating more hot carriers in the metal.

4. Conclusion

In conclusion, we have measured SERS of p-ATP on 2D AgNP array with four different excitation wavelengths, 458, 532, 671 and 785 nm, under "on-resonant"

conditions. The chemical transformation from *p*-ATP to DMAB was observed for all excitation wavelengths. The Raman peak intensity of DMAB increased as the laser intensity increased while the total exposure was kept constant. The hot carriers contributing to the chemical reaction could accumulate and the density could increase at the higher laser intensity. The Raman peaks of DMAB were observed with much lower excitation intensity for 458 nm compared to other excitation wavelengths. We plotted I_{1140}/I_{1080} against the total exposures to estimate the exposure required for completing the chemical transformation at 785, 671, 532 and 458 nm excitations. It was found that I_{1140}/I_{1080} was higher for the higher laser intensity. It was also found that the required exposure was smaller for the shorter wavelength, and the value was smaller by ~10^5 times for 458 nm compared to 785 nm. For the excitation of 458 and 532 nm, the incident light is strongly coupled to the 2D AgNP array, where the large electric field is achieved at the nano-gaps. The electric field of 458 nm penetrates more deeply into the metal, which may be the origin for the enhancement of the hot carrier generation.

ACKNOWLEDGEMENT

NT thank ASCENT program (No. 55) in European Nanoelectronics for financial support to visit Tyndall National Institute. NT thank also Okayama University for the financial support to organize a symposium for plasmonics/SERS. MM acknowledge Renishaw UK for access to InVia Qontor Raman facility.

REFERENCES

1. Barnes, W. L.; Dereux, A.; Ebbesen, T. W. Surface plasmon subwavelength optics. *Nature* **2003**, *424*, 824-830.
2. Fleischmann, M.; Hendra, P. J.; McQuillan, A. J.; Raman spectra of pyridine adsorbed at a silver electrode. *Chem. Phys. Lett.* **1974**, *26*, 163-166.
3. Albrecht, M. G.; Creighton, J. A. Anomalously intense Raman spectra of pyridine at a silver electrode. *J. Am. Chem. Soc.* **1977**, *99*, 5215-5217.
4. Jeanmaire, D. L.; Van Duyne, R. P.; Surface raman spectroelectrochemistry. Part I. Heterocyclic, aromatic, and aliphatic amines adsorbed on the anodized silver electrode. *J. Electroanal. Chem.* **1977**, *84*, 1-20.
5. Inouye, Y.; Kawata, S. Near-field scanning optical microscope with a metallic probe tip. *Opt. Lett.* **1994**, *19*, 159-161.

6. Novotny, L.; Pohl, D. W.; Regli, P. Light propagation through nanometer-sized structures: the two-dimensional-aperture scanning near-field optical microscope. *J. Opt. Soc. Am. A* **1994**, *11*, 1768-1779.
7. Nie, S.; Emory, S. R. Probing single molecules and single nanoparticles by surface-enhanced Raman scattering. *Science* **1997**, *275*, 1102-1106.
8. Kneipp, K.; Wang, Y.; Kneipp, H.; Perelman, L. T.; Itzkan, I.; Dasari, R. R.; Feld, M. S. Single Molecule Detection Using Surface-Enhanced Raman Scattering (SERS). *Phys. Rev. Lett.* **1997**, *78*, 1667-1670.
9. Brongersma, M. L.; Halas, N. J.; Nordlander, P. Plasmon-induced hot carrier science and technology. *Nat. Nanotech.* **2015**, *10*, 25-34.
10. Knight, M. W.; Sobhani, H.; Nordlander, P.; Halas, N. J. Photodetection with Active Optical Antennas. *Science* **2011**, *332*, 702-704.
11. Chalabi, H.; Schoen, D.; Brongersma, M. L. Hot-Electron Photodetection with a Plasmonic Nanostripe Antenna. *Nano Lett.* **2014**, *14*, 1374-1380.
12. Bernardi, M.; Mustafa, J.; Neaton, J. B.; Louie, S. G. Theory and computation of hot carriers generated by surface plasmon polaritons in noble metals. *Nat. Commun.* **2015**, *6*, 7044-7052.
13. Brown, A. M.; Sundararaman, R.; Narang, P.; Goddard III, W. A.; Atwater, H. A. Nonradiative Plasmon Decay and Hot Carrier Dynamics: Effects of Phonons, Surfaces, and Geometry. *ACS Nano* **2016**, *10*, 957-966.
14. Besteiro, L. V.; Kong, X.-T.; Wang, Z.; Hartland, G.; Govorov, A. O. Understanding Hot-Electron Generation and Plasmon Relaxation in Metal Nanocrystals: Quantum and Classical Mechanisms. *ACS Photonics* **2017**, *4*, 2759-2781.
15. Liu, J. G.; Zhang, H.; Link, S.; Nordlander, P. Relaxation of Plasmon-Induced Hot Carriers. *ACS Photonics* **2018**, *5*, 2584-2595.
16. Minutella, E.; Schulz, F.; Lange, H.; Excitation-Dependence of Plasmon-Induced Hot Electrons in Gold Nanoparticles. *J. Phys. Chem. Lett.* **2017**, *8*, 4925-4929.
17. Christopher, P.; Xin, H.; Linic, S. Visible-light-enhanced catalytic oxidation reactions on plasmonic silver nanostructures. *Nat. Chem.* **2011**, *3*, 467-472.
18. Mukherjee, S.; Libisch, F.; Large, N.; Neumann, O.; Brown, L. V.; Cheng, J.; Lassiter, J. B.; Carter, E. A.; Nordlander, P.; Halas, N. J. Hot Electrons Do the Impossible: Plasmon-Induced Dissociation of H_2 on Au. *Nano Lett.* **2013**, *13*, 240-247.

19. Mukherjee, S.; Zhou, L.; Goodman, A. M.; Large, N.; Ayala-Orozco, C.; Zhang, Y.; Nordlander, P.; Halas, N. J. Hot-Electron-Induced Dissociation of H_2 on Gold Nanoparticles Supported on SiO_2. *J. Am. Chem. Soc.* **2014**, *136*, 64-67.

20. Boerigter, C.; Aslam, U.; Linic, S. Mechanism of Charge Transfer from Plasmonic Nanostructures to Chemically Attached Materials. *ACS Nano* **2016**, *10*, 6108-6115.

21. Huang, Y.-F.; Zhu, H.-P.; Liu, G.-K.; Wu, D.-Y.; Ren, B.; Tian, Z.-Q. When the signal is not from the original molecule to be detected: Chemical transformation of *para*-aminothiophenol on Ag during the SERS measurement. *J. Am. Chem. Soc.* **2010**, *132*, 9244-9246.

22. Sun, M.; Huang, Y.; Xia, L.; Chen, X.; Xu, H. The pH-Controlled Plasmon-Assisted Surface Photocatalysis Reaction of 4-Aminothiophenol to *p*,*p*′-Dimercaptoazobenzene on Au, Ag, and Cu Colloids. *J. Phys. Chem. C* **2011**, *115*, 9629-9636.

23. Lantman, E. M. van S.; Deckert-Gaudig, T.; Mank, A. J. G.; Deckert, V.; Weckhuysen, B. M. Catalytic processes monitored at the nanoscale with tip-enhanced Raman spectroscopy. *Nat. Nanotech.* **2012**, *7*, 583-586.

24. Xie, W.; Walkenfort, B.; Schlücker, S. Label-Free SERS Monitoring of Chemical Reactions Catalyzed by Small Gold Nanoparticles Using 3D Plasmonic Superstructures. *J. Am. Chem. Soc.* **2013**, *135*, 1657-1660.

25. Zhang, Q.; Wang, H. Mechanistic insights on plasmon-driven photocatalytic oxidative coupling of thiophenol derivatives: evidence for steady-state photoactivated oxygen. *J. Phys. Chem. C* **2018**, *122*, 5686-5697

26. Wang, H.; Liu, T.; Huang, Y.; Fang, Y.; Liu, R.; Wang, S.; Wen, W.; Sun, M. Plasmon-driven surface catalysis in hybridized plasmonic gap modes. *Sci. Rep.* **2015**, 4, 7087.

27. Huang, Y.-F.; Zhang, M.; Zhao, L.-B.; Feng, J.-M.; Wu, D.-Y.; Ren, B.; Tian, Z.-Q. Activation of oxygen on gold and silver nanoparticles assisted by surface plasmon resonances. *Angew. Chem. Int. Ed.* **2014**, *53*, 2353-2357.

28. Takeyasu, N.; Kagawa, R.; Sakata, K.; Kaneta, T. Laser Power Threshold of Chemical Transformation on Highly Uniform Plasmonic and Catalytic Nanosurface. *J. Phys. Chem. C* **2016**, *120*, 12163-12169.

29. Takeyasu, N.; Yamaguchi, K.; Kagawa, R.; Kaneta, T.; Benz, F.; Fujii, M.; Baumberg, J. J. Blocking Hot Electron Emission by SiO_2 Coating Plasmonic Nanostructures. *J. Phys. Chem. C* **2017**, *121*, 18795-18799.

30. Kang, L.; Xu, P.; Zhang, B.; Tsai, H.; Han, X.; Wang, H.-L. Laser wavelength- and power-dependent plasmon-driven chemical reactions monitored using single particle surface enhanced Raman spectroscopy. *Chem. Commun.* **2013**, *49*, 3389-3391.

31. Dong, B.; Fang, Y.; Chen, X.; Xu, H.; Sun, M. Substrate-, Wavelength-, and Time-Dependent Plasmon-Assisted Surface Catalysis Reaction of 4-Nitrobenzenethiol Dimerizing to *p*,*p*′-Dimercaptoazobenzene on Au, Ag, and Cu Films. *Langmuir* **2011**, *27*, 10677-10682.

32. Ye, J.; Hutchison, J. A.; Uji-i, H.; Hofkens, J.; Lagae, L.; Maes, G.; Borghs, G.; Dorpe, P. V. Excitation wavelength dependent surface enhanced Raman scattering of 4-aminothiophenol on gold nanorings. *Nanoscale* **2012**, *4*, 1606-1611.

33. Kagawa, R.; Takeyasu, N.; Kaneta, T.; Takemoto, Y. Oil-in-water emulsion as fabrication platform for uniform plasmon-controlled two-dimensional metallic nanoparticle array. *Appl. Phys. Express* **2016**, *9*, 075003.

34. Rakić, A. D.; Djurišić, A. B.; Elazar, J. M.; Majewski, M. L. Optical properties of metallic films for vertical-cavity optoelectronic devices. *Appl. Opt.* **1998**, *37*, 5271-5283.

35. Huang, Y.-F.; Wu, D.-Y.; Zhu, H.-P.; Zhao, L.-B.; Liu, G.-K.; Ren, B.; Tian, Z.-Q. Surface-enhanced Raman spectroscopic study of *p*-aminothiophenol. *Phys. Chem. Chem. Phys.* **2012**, *14*, 8485-8497.

36. Beharry, A. A.; Woolley, G. A. Azobenzene photoswitches for biomolecules. *Chem. Soc. Rev.* **2011**, *40*, 4422-4437.

37. Johnson, P. B.; Christy, R. W. Optical Constants of the Noble Metals. *Phys. Rev. B* **1972**, *6*, 4370-4379.

TABLE OF CONTENT

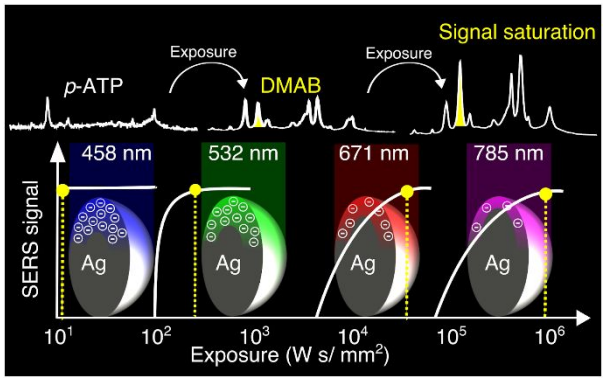

Total exposure required for the signal saturation of DMAB reveals wavelength dependence of hot carrier generation.